ELSEVIER

Atmospheric Research 47–48 (1998) 573–597

ATMOSPHERIC RESEARCH

Exploratory cloud-resolving simulations of boundary-layer Arctic stratus clouds Part I: Warm-season clouds

Peter Q. Olsson [a], Jerry Y. Harrington [a,*], Graham Feingold [c], William R. Cotton [b], Sonia M. Kreidenweis [b]

[a] *Geophysical Institute, University of Alaska in Fairbanks, Fairbanks, AK 99775-7320, USA*
[b] *Colorado State University, Department of Atmospheric Science, Fort Collins, CO 80523, USA*
[c] *Cooperative Institute for Research in the Atmosphere, Colorado State University, NOAA, Environmental Technology Laboratory, 625 Broadway, Boulder, CO 80303, USA*

Abstract

Two-dimensional simulations of arctic stratus clouds (ASC) were conducted using a sophisticated cloud-resolving model with explicit microphysics and a two-stream radiative transfer model. The effects of varying cloud condensation nuclei (CCN) concentrations upon the subsequent cloud and its microphysical, radiative and dynamical structure were studied. In this study CCN concentrations were varied within the ranges found in warm-season arctic boundary layers (ABLs) to produce non-drizzling and weakly drizzling stratus decks. Experiments that included all model physics, no-drizzle, and no shortwave radiation were conducted to elucidate the effects of microphysics and radiation on the simulated stratus. Both simulations that did and that did not include the effects of drizzle showed that the higher CCN concentrations produced a cloud with larger reflectivity and absorptivity, but also produced eddies that were weaker than with lower CCN concentrations. Simulations that included the effects of drizzle showed a similar response to changes in CCN concentrations. Simulations with no drizzle produced more vigorous eddies than their drizzling counterparts because cooling due to evaporation below cloud tends to stabilize the ABL. The simulations without the effects of short-wave radiation produced very vigorous eddies that penetrated more deeply into the ABL. In this case, the simulation with higher CCN concentrations produced the most vigorous eddies. This resulted from a subtle interplay of microphysics, radiation, and dynamics.

Keywords: Arctic stratus clouds; Boundary layer dynamics; Climate—Arctic; Radiation; Cloud microphysics

* Corresponding author.

0169-8095/98/$19.00
PII S0169-8095(98)00066-0

1. Introduction

Recent global climate modeling studies suggest that the Arctic climate tends to be very sensitive to doubling of tropospheric CO_2 concentrations (Walsh and Crane, 1992), with the greatest warming occurring in the Arctic winter season. This so-called 'polar amplification' effect is seen in simulated warming of 8–16°C in the Arctic compared to 1.5–4°C at lower latitudes (Houghton et al., 1992). Unfortunately, the skill in modeling high-latitude climate lags behind that of other regions, casting doubt on the credibility of these results. A major source of uncertainty in global climate models (GCMs) is their inability to adequately predict arctic stratus clouds (ASC) and cloud/surface albedo radiative interactions (Walsh and Crane, 1992). The poor performance of GCMs has been attributed to a number of factors: inadequate vertical and/or horizontal resolution, incorrect latitudinal moisture transport, neglect of aerosols, and incomplete cloud microphysical and radiative transfer schemes, among others. Thus, to achieve more credible climate simulations, it is vitally important to improve the treatment of ASC in numerical models.

ASC over the ice-bound Arctic Ocean tend to be widespread and persistent. With cloud-fractional coverage typically ranging from 0.7–0.9 in the warm season (Herman and Goody, 1976), ASC play an important role in the surface radiation budget in the Arctic. Both the solar and infrared radiative effects of ASC on the regional climate differ from that of stratus clouds at lower latitudes. The Arctic is snow-covered for most of the year giving a surface albedo greater than that of ASC. Hence, any overlying cloudiness tends to decrease the solar radiation reflected back to space. Only during the short summertime melt season does this trend reverse. Curry et al. (1988) found that, with the exception of a few weeks in midsummer, cloud-radiative effects [1] tend to warm the Arctic atmosphere and surface. This contrasts with the typical net cooling associated with stratus in lower latitudes. These abrupt and short-lived seasonal changes in radiative impact have a subtle yet significant impact on the annual high-latitude radiation budget and ultimately a cumulative effect on the long-term evolution of the cryosphere.

A further implication of ASC in climate change involves the strong correlation between cloud condensation nuclei (CCN) concentration and cloud droplet number concentration (N_t, Twomey, 1959). Evidence is mounting (e.g., Barrie, 1986) that the Arctic Basin is a sink region for anthropogenic pollutants transported northward from midlatitude sources. Besides this potential source of CCN and other aerosols, it has been suggested that gaseous pollutants can modify the activation characteristics of in-situ CCN (e.g., Heintzenberg et al., 1986; Shaw, 1986) and ice nuclei (IN, Curry and Ebert, 1992). Since an increase in N_t (modulated for example by CCN concentrations) for a fixed liquid water content produces a more reflective cloud composed of smaller droplets, long-term changes in CCN concentration would feedback on the Arctic radiation budget and ultimately global climate (Curry, 1995). It has been suggested (e.g.,

[1] We use the phrase, 'cloud-radiative effects', rather than the standard, 'cloud-radiative forcings', to describe the effects that cloud/radiative interactions have upon the environment. This is chosen because of potential confusion associated with the word, 'forcing', which has a definite physical meaning.

Stamnes et al., 1995) that a consequence of the increasing anthropogenic aerosol burden seen in the Arctic might be a tendency for cloud drops to become numerous and smaller. This would tend to suppress drizzle, and to the extent that drizzle is responsible for the breakup of stratus decks (Albrecht, 1989; Ackerman et al., 1993), lead to even more persistent ASC coverage.

To understand the arctic climate and correctly predict future climate, it is essential that we gain a better understanding of the interactions among the boundary-layer dynamics, cloud microphysics and radiation which create and maintain ASC. Unfortunately, several issues confound a modeling approach to this task. ASC often coexist in multiple layers (Tsay and Jayaweera, 1984), and are found in a variety of synoptic conditions (Curry and Herman, 1985a). The supporting boundary-layer environment frequently has a complex temperature and shear structure (Curry et al., 1988), rendering typical one-dimensional stratus cloud models (e.g., Lilly, 1968; Randall, 1980) inadequate. The approach taken here is to use cloud-resolving simulations of ASC to examine these interactions and, in particular, to examine the sensitivity of ASC to changes in number concentrations of CCN (N_{ccn}). In Section 2 we describe the model; Section 3 considers the experimental design and sensitivity studies; in Section 4 we present the results of the simulations; and in Section 5 these results are summarized and implications are discussed.

2. Model description

The model used in this study is the two-dimensional analog of the Large Eddy Simulation or LES version of the Regional Atmospheric Modeling System (RAMS), a model developed at Colorado State University (Pielke et al., 1992). This model has been used to examine sensitivity to variations in CCN concentrations (Feingold et al., 1994) and simulate drizzle production in marine stratocumulus (Feingold et al., 1996; Stevens, 1996). As implemented here, the non-hydrostatic model integrates predictive equations for the velocity components (u and w), a perturbation form of the Exner function (π), a total water substance mixing ratio (r_t) and the liquid-water potential temperature (θ_l, Tripoli and Cotton, 1981) on a vertically stretched Arakawa C-grid.

2.1. Bin-resolving microphysics

In our preliminary attempts to simulate precipitating ASC, the autoconversion and sedimentation schemes implemented in the traditional bulk microphysical parameterization of RAMS (Walko et al., 1995) failed to adequately reproduce the drizzle process. This was largely due to the use of the mean radius ($\bar{r}$) of hydrometeors in the statistical representation of the cloud drop spectrum. The small $\bar{r}$ found in the few field observations of ASC (e.g., Curry, 1986) was insufficient to initiate precipitation using traditional bulk autoconversion parameterizations (e.g., Berry and Reinhardt, 1974) although precipitation was observed in those clouds. To address this deficiency, an explicit Bin-resolving Microphysics (BM) model was used (Feingold et al., 1994; Stevens et al., 1996). In BM, 25 drop bins were defined using a mass-doubling formula $x_{k+1} = 2x_k$, covering a radius range of 1.5–500 μm, where x is drop mass. Predictive equations for both mass and number in each bin require a total of 50 prognostic

variables for cloud-related scalars. Moment-conserving techniques that prevent artificial drop growth were used to solve equations for warm microphysical processes: condensation/evaporation (Stevens et al., 1996), stochastic collection (Tzivion et al., 1987) and sedimentation. Droplet activation was based on supersaturation, assumed a simple (although somewhat artificial) constant background N_{ccn} with a fixed lognormal distribution, and N_t bounded above by N_{ccn}. Further details on aerosol composition and activation may be found in Stevens et al. (1996).

2.2. Two-stream radiation model

A new two-stream radiative transfer scheme was implemented in the RAMS-LES model for this work. In this scheme, transfer equations for both solar and infrared radiation are solved for three model gases: $(H_2O)_v$, O_3, and CO_2 which includes average climatological CH_4, O_2 and NO_2 (Ritter and Geleyn, 1992). Gaseous overlap for solar fluxes and net infrared fluxes are computed using fast exponential sum-fitting of transmissions (FESFT, Ritter and Geleyn, 1992; Edwards, 1996) for the band structure of Ritter and Geleyn (1992). Rayleigh scatter and continuum absorption are treated as independent of wavelength (grey) across a given band and are computed with the formulae given by Slingo and Schrecker (1982) and Liou (1992), respectively.

The optical properties of water drops are treated with the methodology of Slingo and Schrecker (1982). Band-averaged values of the single scatter albedo (ω_p) and the extinction coefficient (β_{ext}) are computed and fit as functions of the characteristic diameter (D_n) of a generalized gamma distribution function (Walko et al., 1995). Absorption and extinction cross sections are computed using anomalous diffraction theory (ADT) modified for spheres as discussed in Mitchell (1997). The value of the asymmetry parameter, g, is set at 0.85 for these simulations. While the Eulerian BM model allows the drop distribution to fluctuate freely depending upon external conditions, scattering properties are based on an assumed gamma distribution with a fixed shape parameter (ν). For these simulations $\nu = 6$ was chosen to represent the narrow spectrum typical of weakly drizzling stratus layers. As is shown later, this choice of ν generally agreed with the drop sizes produced by the BM. [2] A more detailed explanation of the radiative transfer model may be found in Harrington (1997).

3. Experiment design

3.1. Case description

The sounding used in this study is derived from a composite of aircraft data taken on 28 June 1980 over the Beaufort Sea as part of the Arctic Stratus Experiment (ASE). A brief synopsis of the case will be presented here. Various aspects of the data acquisition

[2] Currently, a new methodology for incorporating the time-varying distribution of the drop-size spectrum into the computations of the optical properties has been developed (Harrington, 1997).

and reduction and cloud morphology can be found in Tsay and Jayaweera (1984). Detailed discussions of the observed radiative and microphysical properties of the case can be found in Herman and Curry (1984) and Curry (1986) and of boundary layer structure in Curry et al. (1988). It should be recognized that the initial fields used herein represent a composite of a large spatially and temporally varying cloud field with extant vertical motions. The use of this composite structure as a starting point does not suggest that we are doing a 'case-study' simulation, but rather that the initial conditions used here are representative of a 'typical' ASC environment. Therefore, it should not be surprising (or even desirable) that the final mean profiles of our simulated clouds replicate the initial ones.

Fig. 1 shows the horizontally homogeneous initial state of the simulations. The cloud cover (Fig. 1a) consists of two quasi-parallel and continuous stratus decks, the lower (fog) layer extending from the surface to about 270 m ASL with a maximum liquid

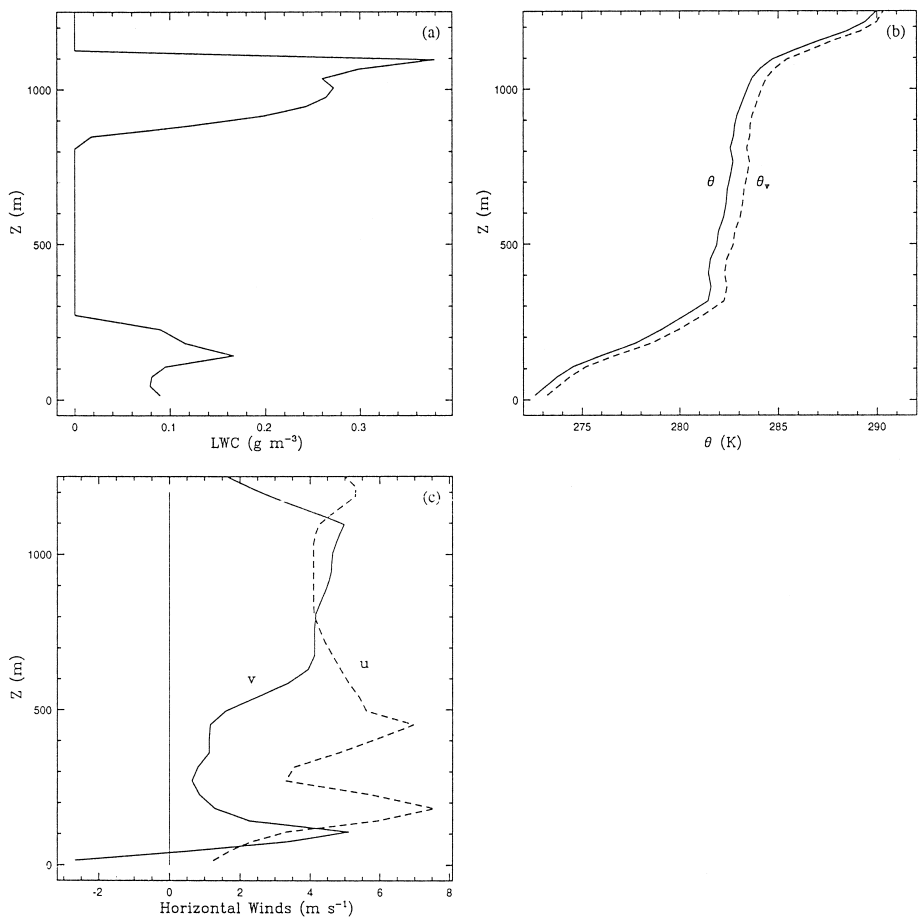

Fig. 1. Mean fields used to produce the initial cloud field: (a) liquid water content (LWC); (b) θ and θ_v; and (c) the u and v winds.

water content (LWC) of about 0.16 g m^{-3}. The upper deck has a base at 800 m with a maximum LWC of 0.38 g m^{-3} near cloud top at 1120 m ASL. The upper deck is capped by a strong inversion (Fig. 1b). From 1100 m down to the top of the fog deck, the temperature lapse rate is nearly moist adiabatic. By contrast, the atmosphere within the fog layer is extremely stable, with a lapse rate near 30 K km^{-1}. The horizontal wind profiles (Fig. 1c) show very strong shear in the lowest 100 m, with a complex shear profile extending from the surface to about 100 m below the base of the upper cloud.

3.2. Model grid structure and boundary conditions

The three-dimensional updraft/downdraft (large-eddy) structure responsible for the variations in supersaturation and observed liquid water content (LWC) in the cloudy marine boundary layer is most accurately represented in the full three-dimensional dynamic framework (Stevens et al., 1996). However, due to the inherent exploratory nature of these explicit ASC simulations, the results presented here are from two-dimensional model integrations. This computationally expedient simplification permitted several sensitivity studies while still maintaining the fundamental integrity of the radiation/microphysics/dynamics interactions.

The simulation domain had a 3600 m horizontal extent and a height of 2880 m. The horizontal grid spacing was a constant 60 m, while the vertical grid spacing varied within the boundary layer from 30 to 45 m, the smallest spacing occurring near the surface and in the top half of the upper cloud deck. Above the cloud, the vertical grid is stretched using the relationship $\Delta z_{k+1} = 1.13\Delta z_k$. This approach permitted better resolution in the regions of interest (near-surface and cloud top) while permitting the upper boundary to be over 1500 m from the cloud. The upper boundary was a rigid lid and a dissipative Rayleigh friction layer was used in the five highest levels of the domain to dampen reflected gravity waves. For all the simulations, the lateral boundary conditions are cyclic, and non-inertial (coriolis) effects are neglected. The lower boundary was assumed to be sea ice initially in thermal equilibrium with the lowest atmospheric level.

3.3. Sensitivity studies

Few measurements of CCN have been conducted in the Arctic. Relatively little is known about the chemical and physical character of arctic CCN, or of typical N_{ccn} and N_t in the Arctic. Mean N_t measurements taken within a 17-day period during ASE show considerable variability, ranging from 73 to 351 drops (Tsay and Jayaweera, 1984). Saxena and Rathore (1984) reported values near 1000 cm^{-3} for N_{ccn} over the Arctic Ocean. In dramatic contrast, Hegg et al. (1995) analyzed aircraft data taken over the Arctic Ocean in April, 1992 during the Arctic Leads Experiment (LEADEX) and found CCN concentrations (active at 1% supersaturation) ranging from 20 to 93 cm^{-3}, with a mean value of 47 cm^{-3}. These different studies taken together suggest a significant variability in the CCN concentration over the Arctic Ocean.

Table 1
Summary of model simulations

Name	N_{ccn} (cm^{-3})	Microphysics	Radiation	Time period
NM		Supersaturation condensed	SW and LW	0–4 h
100A	100	All	SW and LW	4–6 h
500A	500	All	SW and LW	4–6 h
100ND	100	No drizzle or collection	SW and LW	4–6 h
500ND	500	No drizzle or collection	SW and LW	4–6 h
100NS	100	All	LW only	4–6 h
500NS	500	All	LW only	4–6 h

A number of numerical studies of the microphysical impact of varying CCN concentration (e.g., Feingold et al., 1994) found that increasing CCN numbers resulted in increasing N_t and decreasing effective radius of the cloud droplets. To study potential effects on ASC due to changing CCN concentration, several sensitivity tests were conducted using the bin microphysics and the 4 h 'no microphysics' fields (see discussion in Section 4) as a common point of departure. The sensitivity studies include CCN concentrations of 100 cm^{-3} and 500 with all physics included (denoted 100A and 500A, respectively). To isolate the impact of the drizzle process, complementary runs (100ND and 500ND) were performed with the collection and sedimentation mechanisms disabled in the microphysical parameterization. Runs denoted 100NS and 500NS included all physics except the effects of shortwave (SW) radiation. A summary of the runs is given in Table 1.

4. Results

4.1. Initial spin-up

To introduce an initial inhomogeneity, a random potential temperature perturbation ($-0.1 < \theta' < 0.1$) was imposed in the lowest 1100 m of the domain. The initial thermal profile (Fig. 1b) was stable with respect to saturated vertical motion near the cloud top. During the first 4 h of the simulation, the model was integrated until radiative cooling had destabilized the cloud, allowing vertical circulations (eddies) to develop. To minimize computational time, it was assumed that any supersaturation was immediately condensed in this 'no microphysics' (NM) run. Since the radiative transfer model requires drop size and concentration information, and the NM simulation predicts LWC only, N_t was fixed at 100 cm^{-3} for the duration of the simulation. Other than the energetics associated with phase transformations and radiative interactions, the condensate was assumed passive and no microphysical processes (e.g., collection, sedimentation) were permitted.

The simulation was started at 1000 (local time) on 28 June. After about 2.5 h of simulation time, the net cloud-top cooling rate of $-4.6°$ K h^{-1} had produced sufficient

negative buoyancy to initiate eddies penetrating through the depth of the upper cloud. Fig. 2b shows the total, [long-wave (LW) and solar (SW) heating rates] 4 h into the NM simulation. On this date at 78°N, the sun is above the horizon 24 h a day. While the sun angle is low in the Arctic even near the summer solstice, solar warming of the cloud at midday is still significant and partially counteracts the infrared cooling. The total radiative heating (solid line) is dominated by LW cooling at cloud top and by SW warming in the lower 75% of the upper cloud. The cloud-top cooling also has increased the LWC maximum (Fig. 2a) in the upper cloud by about 20% in 4 h.

In contrast to the initial local maximum in LWC of 0.18 g m^{-3} at 150 m ASL, 4 h later, a local minimum exists at 150 m, the lower cloud no longer extends to the surface, and the liquid-water path of the lower cloud has decreased by about one half. While the LWC in the lower cloud layer at 4 h is about 25% that of the upper cloud, radiative

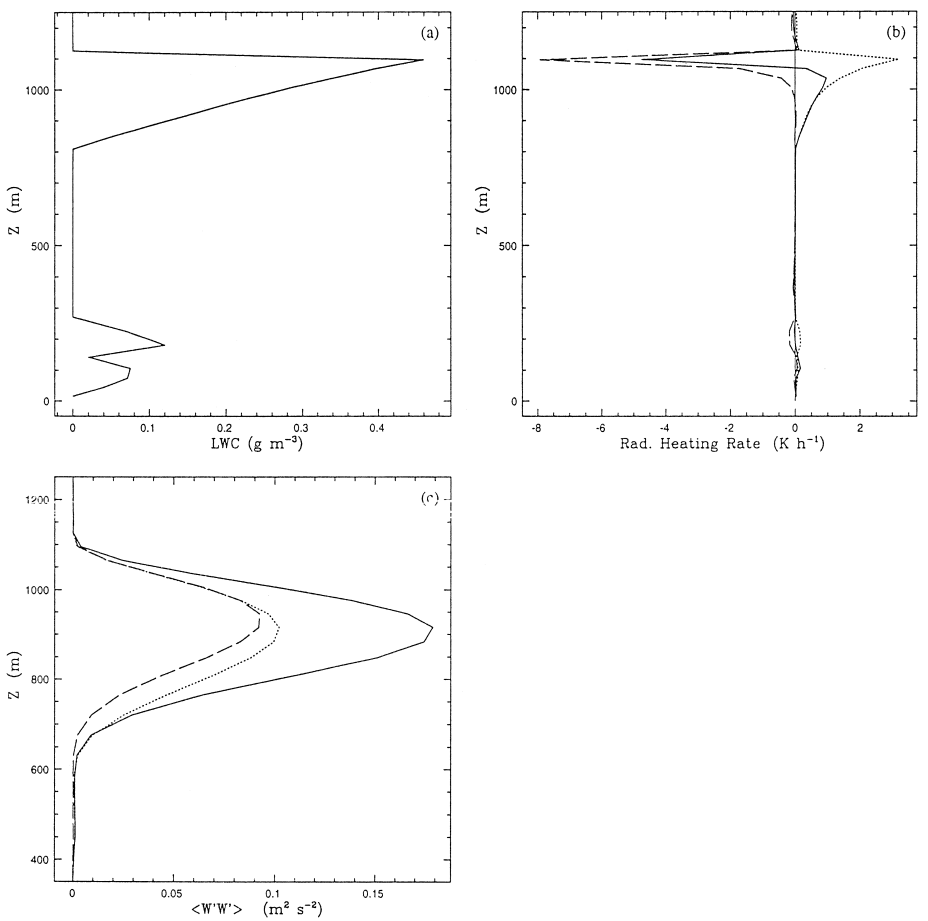

Fig. 2. NM fields at 4 h: (a) LWC; (b) total heating rate (solid line), long wave cooling (dashed line) and shortwave heating (dotted line); (c) $\langle w'w' \rangle$ for NM (solid line), 100A (dotted line) and 500A (dashed line).

heating in the lower deck is more than an order of magnitude less due to the shading effect of the upper cloud and the similar temperatures of both cloud decks. The upward LW flux from the surface is only about 12 W m^{-2} less than the upward LW flux at the top of the lower deck and the albedo of the underlying sea-ice surface is quite similar to that of the cloud. Therefore, from the standpoint of radiation energetics, it would seem that the presence or absence of the lower cloud deck is of relatively little consequence to the dynamics of the upper cloud (though of course the radiative impact of the upper cloud on the lower cloud is very significant).

The horizontal mean vertical velocity variance profile ($\langle w'w' \rangle$, solid line in Fig. 2c) achieved a quasi-steady state by hour 4, with a mid-cloud maximum of 0.2 m^2 s^{-2}. This is consistent with Curry (1986) who found values of $\langle w'w' \rangle$ ranging from 0.08 to 0.16 m^2 s^{-2} in the upper cloud. The somewhat larger vertical velocity variance may be a result of the two-dimensional geometry and could also be due to our somewhat 'idealized' sounding (Stevens, 1996). Curry's results also do not show a mid-cloud maximum. A cross-section of the vertical velocity at four hours of simulation time (Fig. 3) shows a well developed updraft–downdraft structure in and below the upper cloud deck, extending almost 200 m below cloud base. The maximum magnitude of simulated vertical motion at 4 h in the lower deck is less than 0.1 m s^{-1}, in contrast to the vertical motions exceeding 1.0 m s^{-1} in the upper cloud. The very small heating rates in the

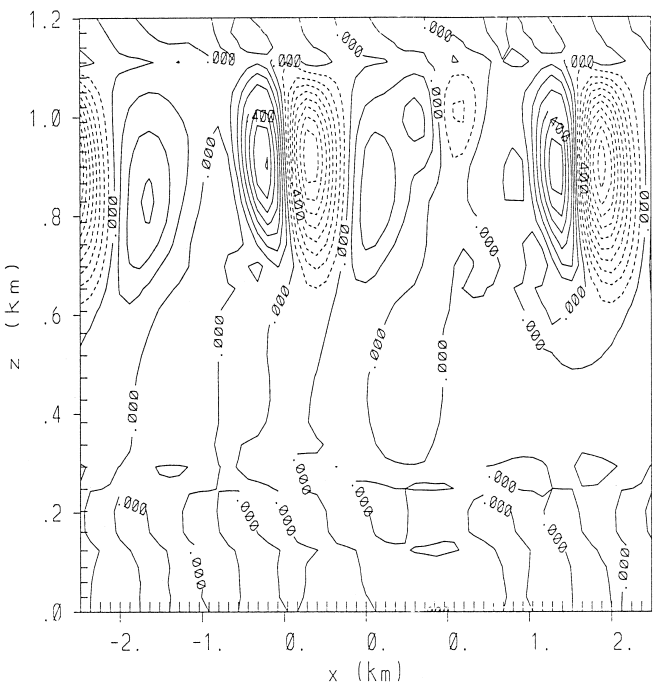

Fig. 3. Vertical velocity (w) in the cloudy boundary layer after 4 h of simulation time. Contour interval is 0.1 m s^{-1} with maximum and minimum vertical motions of $+0.7$ m s^{-1} and -1.0 m s^{-1}, respectively.

lower cloud, coupled with the initial large static stability, suggest that buoyant production of turbulence kinetic energy (TKE) is minimal. The initial horizontal wind profile contains a very large wind shear (greater than 0.07 s^{-1}). Such strong shear provides a large source of mechanically generated turbulence and was likely responsible for the observed value of $\langle w'w' \rangle$ about 2 orders of magnitude larger than in the simulation.

The implicit assumption of a large-scale pressure gradient in geostrophic balance with the initial winds, coupled with cyclic boundary conditions, make it impossible for the model in its current configuration to maintain a shear-driven instability. This would require a much more complex three-way initial balance between the pressure gradient force, coriolis force, and the viscous shear stress, and additionally require that the shear-induced velocity tendencies be calculated from the 'unbalanced shear' only. Perhaps more fundamentally, the two-dimensional framework and 30 m vertical grid-spacing used for these simulations are not adequate to faithfully reproduce such shear-driven turbulence. The potential temperature profile (Fig. 1b) suggests that the lower cloud is decoupled from the upper cloud dynamically. The large stability in the lowest 300 m should strongly inhibit vertical fluxes of water substance, heat and momentum into the more neutral layer overlying the lower cloud deck.

Ultimately, it is difficult to gauge the impact of this deficiency on the fidelity of the simulation since we do not have any comparative observations of how such a specific cloud deck had evolved from the (composite) initial state. For this reason and in light of the probable dynamic and radiative decoupling of the upper cloud deck from the lower, the rest of this paper will focus on the evolution and structure of the upper cloud deck.

4.2. Properties of the 'all microphysics' (A) simulations

The effect of varying the CCN concentration (N_{ccn}) on the mean structure of the simulated ASC layer is shown in Fig. 4 for 100A and 500A with NM also shown for comparison [3]. For a given LWC, a cloud with large N_t would be expected to produce less drizzle and, therefore, have larger cloud top reflectivities relative to a cloud with small N_t. As seen in Fig. 4, larger values of N_{ccn} in the A simulations lead to larger cloud top LWC values (0.47 g m^{-3} vs. 0.38 g m^{-3}), much larger N_t (180 cm^{-3} vs. 50 cm^{-3}) and thus smaller droplets for 500A (Fig. 4d). Throughout the 500A cloud, the effective radius r_e is about 5 μm smaller in 500A than in 100A, since the available liquid water is distributed over a larger number of activated CCN. Profiles of N_t (Fig. 4b) for both cases are approximately constant with height similar to Curry (1986) and other stratocumulus observations (e.g., Nicholls, 1988). Aircraft observations on this day (Tsay and Jayaweera, 1984) found considerable variation in N_t (200–400 cm^{-3}) and encountered sporadic precipitation beneath the cloud layer.

[3] In this and all other subsequent profiles, variables have been averaged over the last hour of the simulation (hour 5 to hour 6) to provide a more representative profile than individual snapshots would provide.

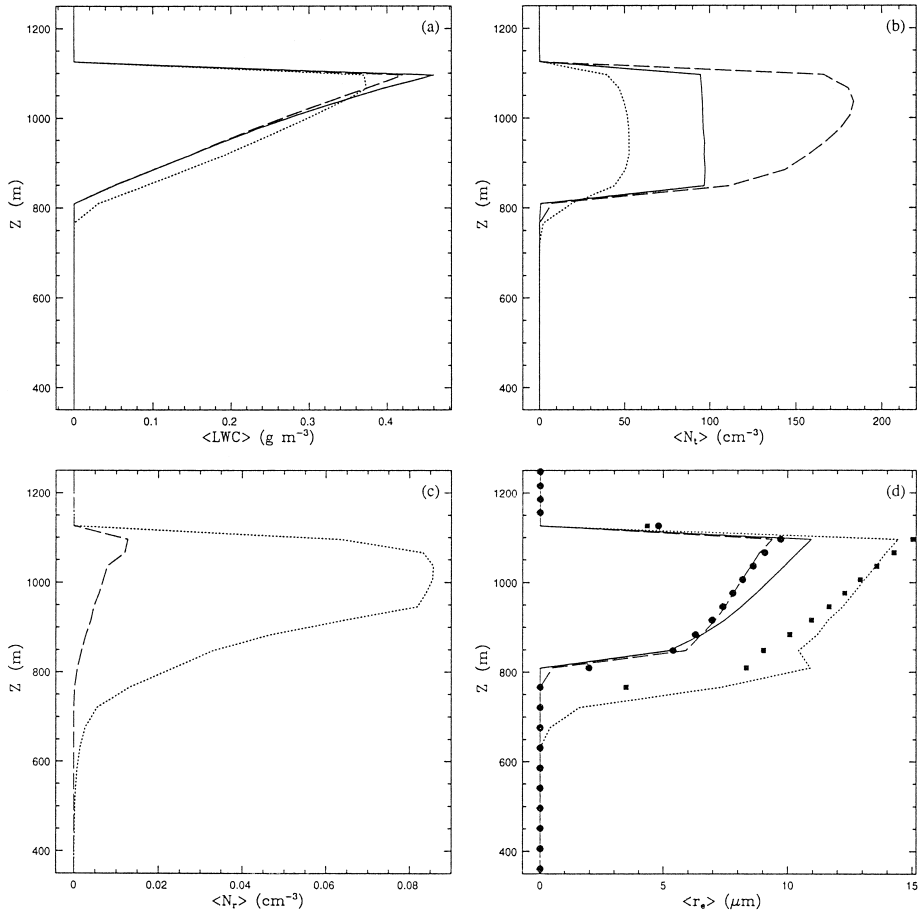

Fig. 4. Microphysical profiles for A and NM simulations. Profiles are temporally averaged over the last hour of the simulation in this (and subsequent figures): (a) LWC; (b) total concentration (N_t); (c) drizzle concentration (N_r); and (d) effective radius (r_e) for NM (solid line), 100A (dotted line) and 500A (dashed line). Points plotted in the r_e profile are derived from assumed gamma ($\nu = 6$) for 100A (squares) and 500A (spheres). Values of N_r for 500A have been multiplied by 1×10^2 to facilitate comparison.

Considering drizzle as droplets with $r > 25$ μm [4], we can define a drizzle droplet concentration (N_r). Profiles of N_r (Fig. 4c) illustrate that an environment with fewer available CCN produces clouds with more drops in the drizzle portion of the spectrum. These profiles, along with the r_e values, indicate an active drizzle process in 100A but not in 500A.

Values of r_e derived with the gamma distribution used to compute the optical properties, compare well with the bin-computed profiles (Fig. 4d) throughout the

[4] We will delineate drizzle droplets as those with radii greater than 25 μm as these drops have significant collection efficiencies (greater than 0.2) and may have sizeable sedimentation velocities.

uppermost 150 m of the cloud in 100A and throughout the entire cloud in 500A. These results suggest that optical properties computed with the gamma distribution function should represent those of the bin microphysics (Hu and Stamnes, 1993) adequately.

From the standpoint of radiation properties, the 500A case compares best to the observations of Curry (1986), which might be expected since N_t in 500A is closer to Curry's observed values. Infrared fluxes computed by the model (Fig. 5a) are close to those presented in Curry and Herman (1985b) with upwelling and downwelling LW fluxes near cloud top of 325 W m^{-2} and 215 W m^{-2}, respectively while LW fluxes at cloud base are about 327 W m^{-2}. Our simulated ASC has an IR flux emissivity of 0.97, well within the observed range of 0.95 to 1.00 (Curry and Herman, 1985b). Comparison of the solar fluxes to the observed values (Herman and Curry, 1984) shows that

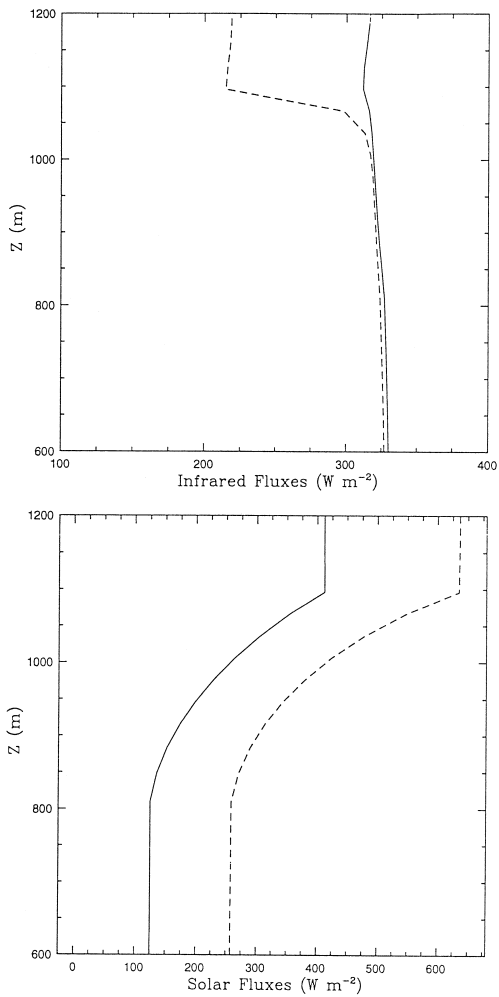

Fig. 5. Profiles of radiative fluxes for 500A. Downwelling fluxes are denoted by the dashed line while upwelling fluxes are denoted with the solid line.

downwelling and upwelling solar fluxes are a few watts per square meter greater at the top of the simulated cloud. Fluxes near cloud base are somewhat smaller indicating that stronger attenuation is occurring within the simulated system.

Table 2 shows that cloud reflectivities are much lower in 100A (0.495) than in 500A (0.544). Even though the 500A cloud layer reflects more radiation, the increased optical paths due to scattering allows for slightly more overall absorption in this case (0.116 as compared to 0.115 in 100A). Most of this absorption occurs near cloud top through the larger net flux divergence in 500A. Measured reflectivities (~ 0.6) and absorptivities (~ 0.06) shown in Herman and Curry (1984) illustrate that the observed cloud was more reflective and less absorptive than the simulated ASC.

In conjunction with these results, radiative heating and cooling rates attain greater maxima and are more concentrated near cloud top in 500A as is shown in the liquid water potential temperature (θ_l) tendency panels of Fig. 6. Cloud top cooling rate maxima, between -4 and -5.5 K h^{-1}, are lower and heating rate maxima, between 0.6 and 1.1 K h^{-1}, are greater than the modeling results presented in Curry (1986). The biggest difference appears to be the stronger SW heating rates that occur in these cases.

As this ASC case is driven strongly by cloud top radiative cooling (Curry et al., 1988), and since the radiative effects impact the θ_l budget, processes that offset the destabilizing effects of cloud top radiative cooling will affect cloud evolution (Fig. 6). Impacts of the various processes on θ_l (Betts, 1973), which is conservative for phase change processes but not for precipitation processes, quantifies the potential for a given process to heat/cool the local environment. This gives information about the importance of that process in the overall cooling (called equivalent heating in Frisch et al., 1995 and Feingold et al., 1996). The radiative cooling and heating strongly affect the total energy budget of the cloud layer (Fig. 6c). The 100A case shows much stronger cooling of the entire layer than 500A because the stronger SW heating in 500A is not offset as substantially by cooling processes as in 100A. Cloud top radiative cooling is largely offset by microphysical processes in 100A, but through both microphysics and diffusion in 500A. Overall, cloud top is cooled much more strongly in 500A as shown in Fig. 6c because cloud-top heating effects are not as large. Larger drizzle rates in 100A increase the evaporative cooling of drops beneath cloud base, thus leading to stabilization of the layer. The cooling of the lower portions of the cloud must be maintained against the SW radiative heating which helps to stabilize the cloud. In 100A, microphysical, advective and diffusive processes substantially offset this heating whereas in 500A, even though diffusive cooling is much larger, the effect is less pronounced (compare $\mathrm{d}\theta_l/\mathrm{d}t$ for each case) resulting in much stronger overall heating in this case.

Table 2
Reflection (R_0), transmission (T_0) and absorption (A_0) functions for simulated clouds derived as per Herman and Curry (1984)

	100A	500A	100ND	500ND
R_0	0.495	0.544	0.526	0.586
T_0	0.390	0.340	0.363	0.298
A_0	0.115	0.116	0.111	0.116

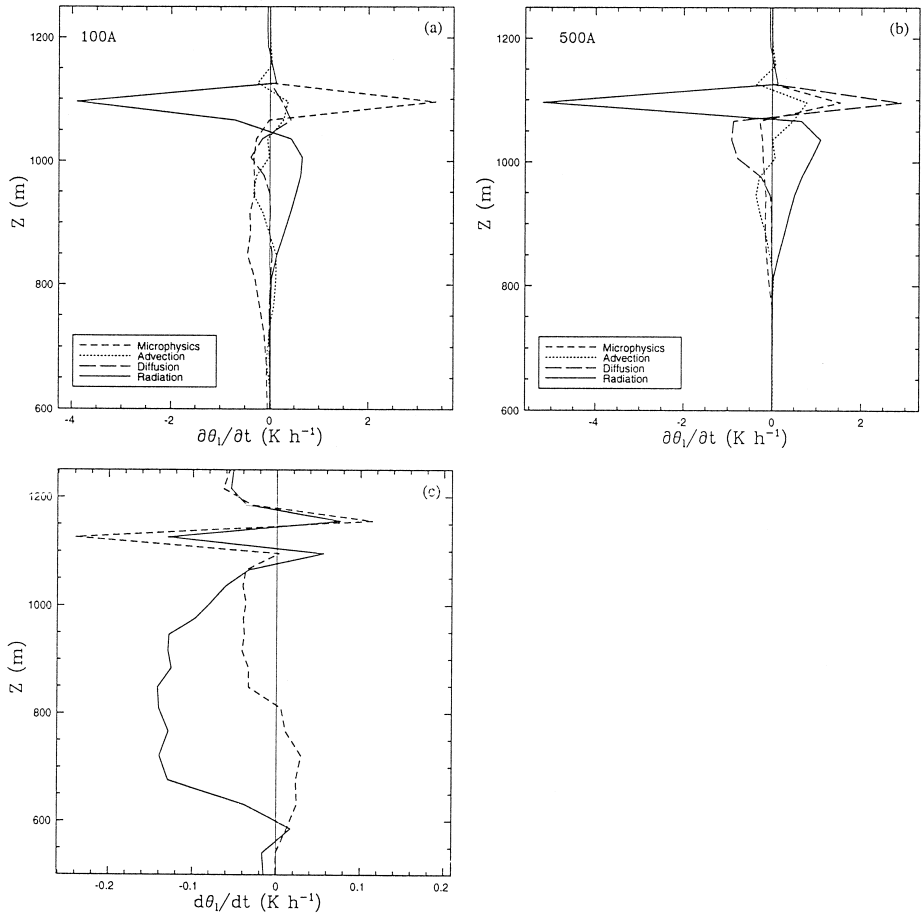

Fig. 6. θ_l tendencies for the A simulations: (a) contributions from the various model components to the θ_l tendency for 100A; (b) as in (a) but for 500A; (c) total θ_l tendency for 100A (solid line) and 500A (dashed line).

Parcels radiatively cooling within the mixed-layer become negatively buoyant and generate TKE (Deardoff, 1981). Consequently, radiative cooling that occurs in this region should be readily mixed throughout the cloudy layer. In order to determine the significance of this process in each case, the amount of cooling which occurs within the mixed-layer and the inversion zone is determined (Deardoff, 1981). This is accomplished by integrating the cooling rate profile throughout the mixed layer (C_M), the inversion zone (C_I) and throughout the cloud for radiative heating (H). The results appear in Table 3. Radiative cooling occurs over a more shallow depth for large N_t, and therefore 500A shows a much greater fraction of the overall cooling in the inversion layer. Since the near cloud-top cooling extends through a greater depth in 100A, more cooling is readily available for negative buoyancy generation in the mixed layer. In

Table 3
Radiative cooling rates integrated within the mixed-layer (C_M), the inversion (C_I) and the total integrated radiative heating (H)

	100A	500A	100ND	500ND	100NS	500NS
C_I (K h^{-1} m)	−67.3	−90.0	−73.2	−87.7	−165.8	−237.0
C_M (K h^{-1} m)	−66.3	−56.7	−60.3	−60.2	−136.3	−66.5
H (K h^{-1} m)	77.0	118.3	80.35	119.0	1.772	5.78
Total (K h^{-1} m)	−56.6	−28.4	−53.15	−28.9	−300.38	−297.92

conjunction with this greater in-cloud cooling, 100A also has smaller integrated solar heating rates. Net radiative effects, therefore, cool the cloud layer more in 100A than in 500A, accounting for the differences in total cooling rates ($d\theta_l/dt$). This result agrees with subtropical stratocumulus studies (Nicholls, 1988) where incorporation of radiatively cooled air into downdrafts was found to be the primary mechanism for cooling and negative buoyancy production.

The total cooling of the layer in 100A is great enough to cause significant decreases in θ_v [5] over time in comparison to 500A (Fig. 7). The weaker overall cooling in 500A produces a cloud which is, overall, warmer than that in the 100A case. The reduction in θ_v for 100A through radiative effects causes greater buoyancy production of $\langle w'w' \rangle$ and, thus, more vigorous circulations (greater $\langle w'w' \rangle$, Fig. 2) in that case. Since θ_v and r_v (not shown) increased throughout the 500A cloud layer as compared to the 4-h values, buoyancy is suppressed in comparison to 100A and the eddy strength is commensurately lower. Circulation strengths in both 100A and 500A are weaker than the 4-h NM profiles (Fig. 2) because drizzle, as shown in Fig. 6, tends to stabilize the cloud layer (Stevens, 1996).

The model generated buoyancy production maxima between 2×10^{-4} and 3×10^{-4} m^2 s^{-3} are somewhat greater than aircraft-derived values near 1.6×10^{-4} m^2 s^{-3} (Curry et al., 1988). Buoyancy production of $\langle w'w' \rangle$ in the model is the dominant term, which is consistent with the results of Curry et al. (1988).

4.3. Simulations with no sedimentation (ND)

Comparison of the profiles for ND (Fig. 8) and A (Fig. 4) show that the effect of the drizzle sedimentation process on cloud microphysical structure is minimal. Liquid water contents are similar among the cases and only the drizzle characteristics of 100A show much difference. Production of drizzle-sized droplets in ND is much weaker, with the largest amounts occurring at cloud top. Surprisingly, the r_e profiles are similar between A and ND, the largest difference being the lack of a cloud base maximum in 100ND as compared to 100A. Values of r_e derived with the gamma distribution function used in the radiative calculations again show good agreement with the bin-derived values,

[5] We use the virtual potential temperature $\theta_v = \theta(1 + 0.61 r_v)$ in this analysis to include the buoyancy effect resulting from horizontally inhomogeneous water vapor content.

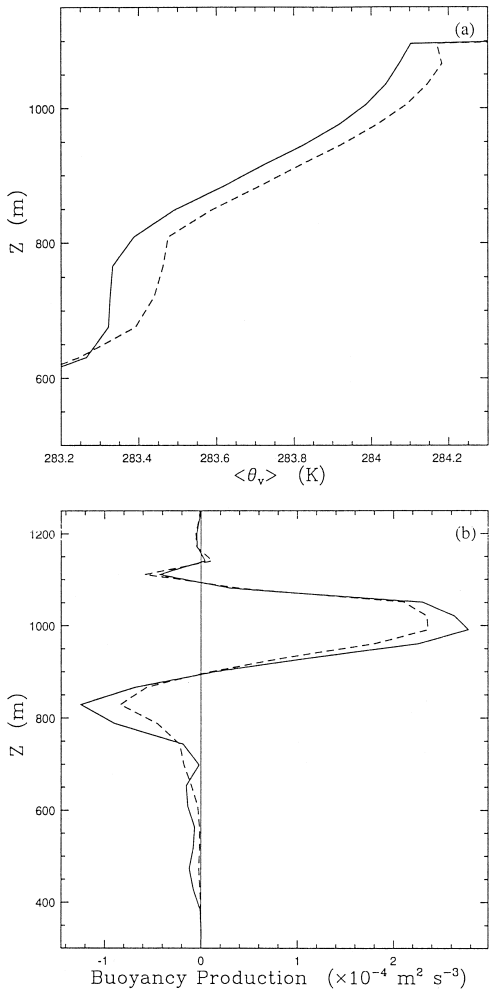

Fig. 7. Profiles of (a) θ_v and (b) buoyancy production (solid line for 100A and dashed line for 500A) for the A simulations.

suggesting the appropriateness of the optical property calculations (see Harrington, 1997 for a more detailed discussion).

Without sedimentation, both cloud layers become more reflective, and less transmissive (Table 2) as fewer large drops are produced. Total solar absorption is reduced in the 100ND case, but there is almost no difference between 500A and 500ND since little drizzle is produced in 500A anyway. The impact of sedimentation on the radiative properties produces only a small effect on the radiative heat budget, with the ND radiative heating rates (Fig. 9a) being quite similar to those produced in the A cases (Fig. 6a and b). Furthermore, Table 3 shows similar integrated heating and cooling is occurring in ND as in A. The greater SW heating in 500ND, as compared to 500A, leads

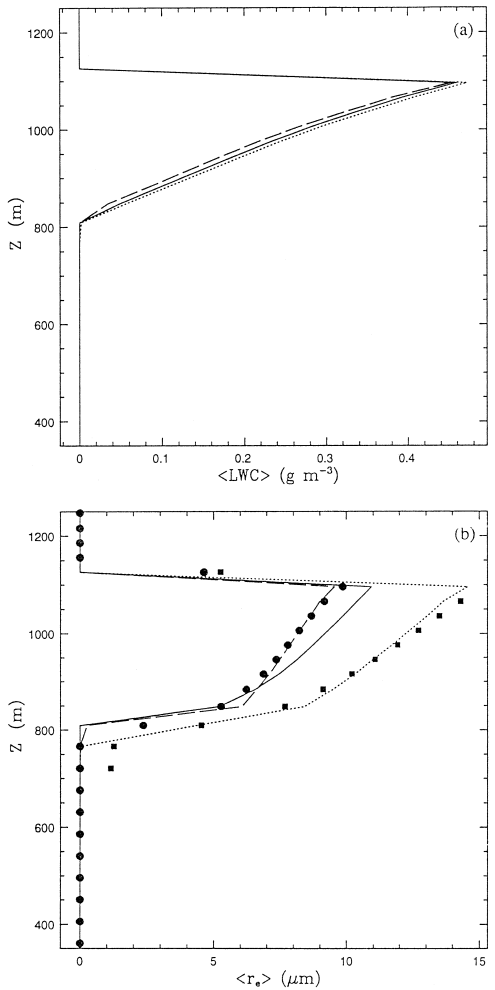

Fig. 8. Microphysical profiles for ND simulations: (a) LWC; and (b) effective radius (r_e) for simulations NM (solid line), 100ND (dotted line) and 500ND (dashed line). Points plotted in the r_e profile are derived from an assumed gamma ($\nu = 6$) for 100ND (squares) and 500ND (spheres).

to smaller in-cloud cooling rates ($d\theta_l/dt$, Fig. 9b) and, therefore, a similar stabilizing effect for larger N_{ccn}. Thus, differences in the θ_v profiles (Fig. 9c) along with buoyancy production of $\langle w'w' \rangle$ (Fig. 9e) are similar to the A cases. Without the stabilizing effects of drizzle, however, buoyancy production rates in ND become larger as do the circulation strengths ($\langle w'w' \rangle$) compared to those in the respective A cases (cf. Fig. 2c). A difference between the strength of the circulating eddies in 100ND and 500ND still remains because of the stronger SW heating for the larger N_t. Ultimately, the main effect of sedimentation on the simulated ASC is stabilization of the subcloud layer (for an in-depth discussion of this, see Stevens, 1996). It is noteworthy that even in 500A, which produced very low drizzle amounts, the effect of this stabilization is apparent.

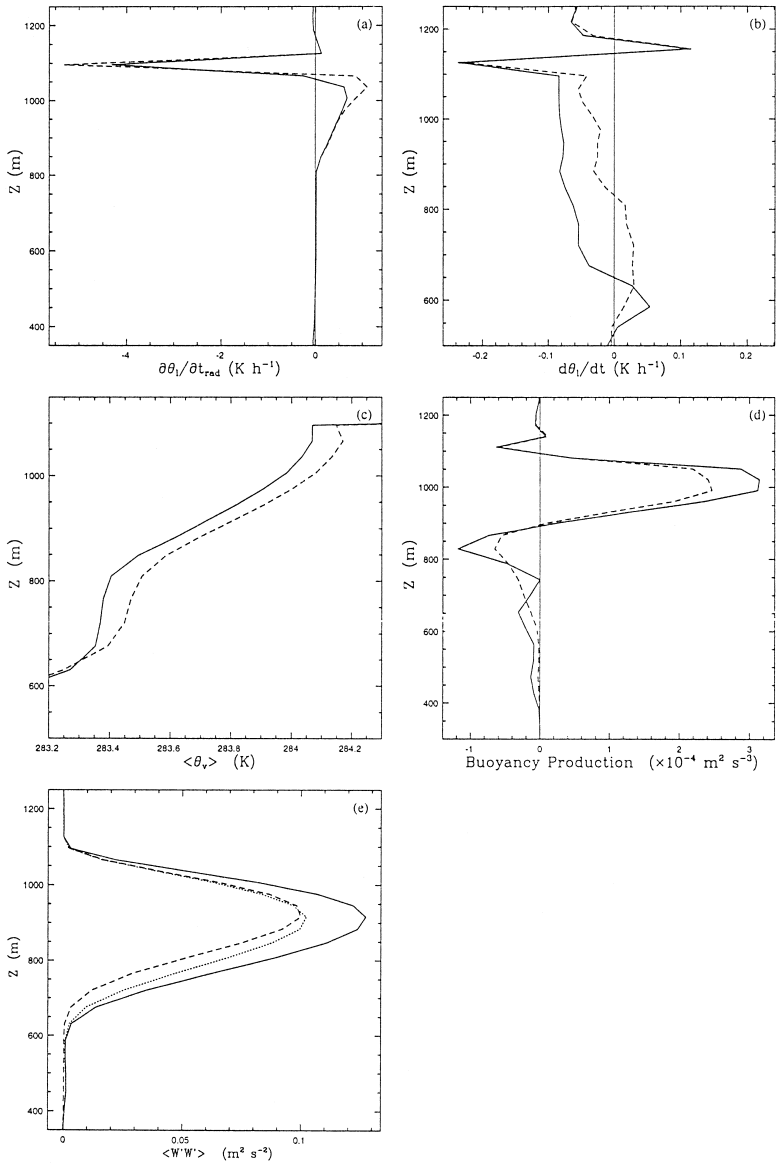

Fig. 9. Thermodynamic and dynamic profiles for ND simulations: (a) radiative heating rate ($\partial\theta_l/\partial t_{rad}$); (b) total θ_l tendency ($d\theta_l/dt$); (c) θ_v; (d) buoyancy production; and (e) $\langle w'w' \rangle$ (solid line for 100ND, dashed line for 500ND, dotted line for 100A).

4.4. Simulations without shortwave radiation (NS)

Results presented thus far suggest that SW radiation absorption appears to have a strong stabilizing effect on the ASC layer. This is important for stratus in the Arctic

environment because of the large impact of continuous SW heating. Simulations without solar radiation (NS) give an indication of just how strong an effect SW absorption has. A comparison of Figs. 10 and 4 shows that the lack of SW heating has a substantial impact on the microphysical structure of the cloud layer. The depths and LWC of the clouds are significantly increased in NS, with 500NS producing a higher cloud top through radiative encroachment (Deardoff, 1981). Total drop concentrations (N_t) have increased in both 100NS and 500NS due to increased mixing and cooling (see below) which allows for enhanced drop activation, and 100NS r_e values near cloud base are also substantially increased. The 500NS case, however, produces little difference in r_e profiles compared to 500A, indicating that even though greater condensation is occurring in 500NS, drop concentrations are too high to allow initiation of significant drizzle.

Since no SW heating occurs and LWC has increased, NS cloud-top radiative cooling rates are larger and extend through a greater depth of the cloud (Fig. 11a and b). Further

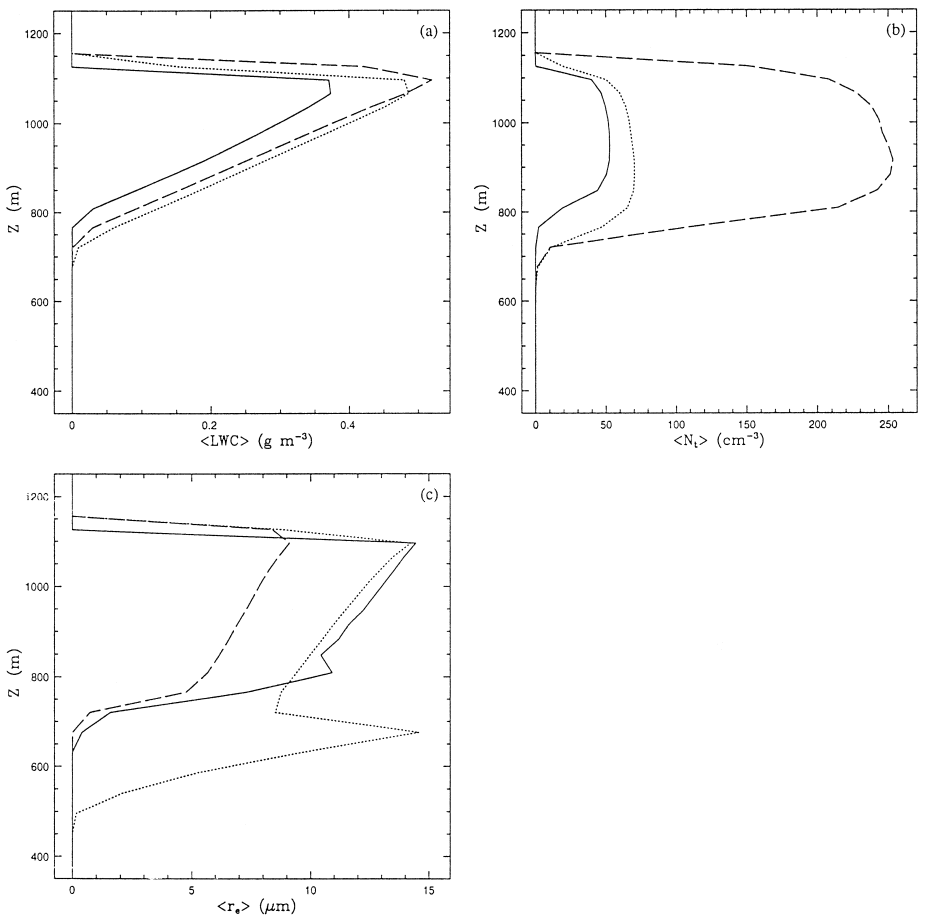

Fig. 10. Microphysical profiles for NS simulations. (a) LWC; (b) total concentration (N_t); and (c) effective radius (r_e) for 100A (solid line), 100NS (dotted line) and 500NS (dashed line).

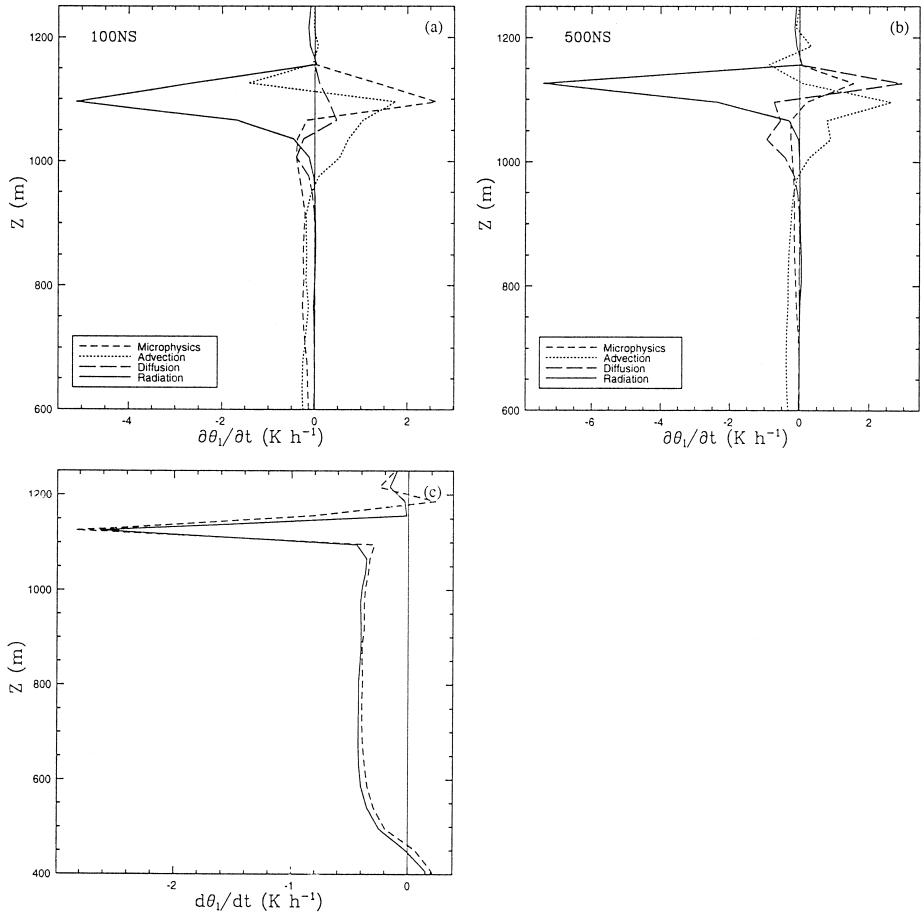

Fig. 11. As in Fig. 6 but for the NS simulations

condensation above the initial cloud top in 500NS occurs because a large portion of the LW cooling occurs here (-237 K h^{-1} m as compared to -165 K h^{-1} m for 100NS). Mixed-layer radiative cooling is, again, much greater in 100NS with values of -136.3 K h^{-1} m compared to -66.5 K h^{-1} m in 500NS. A small amount of LW heating within the lower portions of the cloud occurs in both cases. Overall, the stronger radiative cooling of the mixed-layer in the NS simulations produces larger net cooling of the cloudy layer, reducing θ_v (Fig. 12a). Differences in thermodynamic structure between the 500NS and 100NS cases are minimal, suggesting that the dependency of SW heating on N_t plays a dominant role in the differing thermodynamic structures of 100A and 500A.

In NS, the long-wave radiative destabilization of the cloud layer has no compensating stabilization from SW heating. Consequently, buoyancy production of $\langle w'w' \rangle$ increases by over a factor of 2 in NS, resulting in stronger and more deeply penetrating eddies.

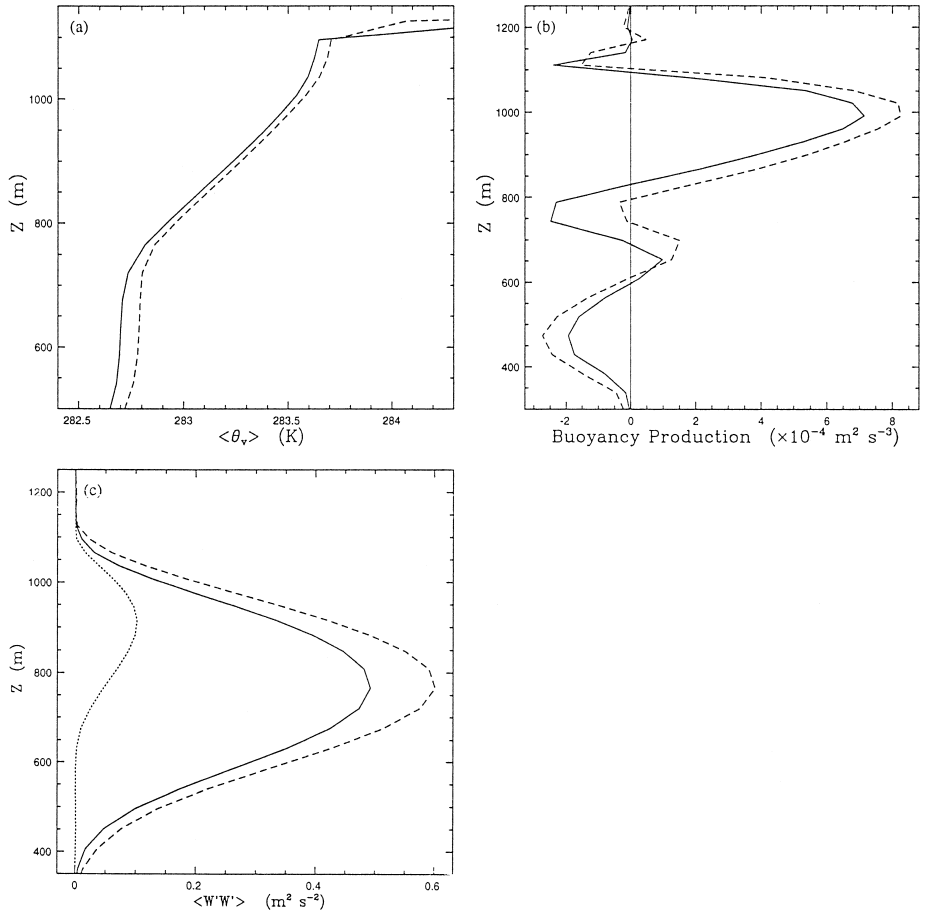

Fig. 12. Profiles of (a) θ_v, (b) buoyancy production, and (c) $\langle w'w' \rangle$ (solid line for 100NS, dashed line for 500NS, and for comparison, dotted line for 100A).

Buoyancy production is reduced in 100NS over 500NS and, as all other thermodynamic tendencies are similar, must be due to the stabilizing effects of stronger drizzle production in this case (Fig. 11). A comparison with the A simulations suggests the stabilization due to SW absorption is more important than the stabilizing effect of the drizzle process, at least for the weakly drizzling conditions simulated here. The 100A case had both drizzle and SW heating acting as stabilizing agents, yet the stronger SW heating in 500A resulted in weaker circulations than 100A even though drizzle-induced stabilization was larger. Also, because SW stabilization occurs in the vicinity of the buoyancy production maximum, circulations tend to become more shallow, as downdrafts are the primary forcing mechanism (Nicholls, 1988). This effect may not typically be as pronounced in ASC as in subtropical stratocumulus (Rogers and Koračin, 1992). In lower latitude stratocumulus, SW heating can decouple the cloud and subcloud layers,

thus isolating the cloud deck from surface fluxes that contribute significantly to the cloud layer buoyancy. In the case presented here, the upper cloud layer is already decoupled from the surface by the strong surface inversion.

5. Summary and conclusions

The simulated ASC showed reasonable agreement with observations taken for the 28 June 1980 ASC case. Simulations with larger CCN concentrations compared most closely to observations, with the exception, perhaps of drizzle; observations of this case reported intermittent drizzle at cloud base (Tsay and Jayaweera, 1984, although quantitative analysis is not given) whereas the simulation with larger CCN concentrations produced little drizzle at cloud base. Eddies were stronger than observed but a cloud base maximum in $\langle w'w' \rangle$ similar to observations (Curry, 1986) was simulated. Sensitivitiy studies showed the importance of radiative–microphysical–dynamical interactions in ASC.

- N_{ccn} affects eddy strength through the modulation of drizzle production; lower N_{ccn} enhances drizzle production resulting in subcloud stabilization and concomitant decreases in $\langle w'w' \rangle$.
- SW heating has an even more dominant stabilizing effect than drizzle.
- Solar radiation impacts the dynamics and, hence, the microphysics and thermodynamics in two specific manners. The first is through control of the strength of the destabilization of the cloud top while the second is through control of the depth of the cloud-scale mixing (and, thus on the location of the $\langle w'w' \rangle$ maximum). The effect is similar to that in marine stratocumulus (e.g., Rogers and Koračin, 1992), however, since the ASC here are effectively decoupled from surface fluxes at any rate, the effects of SW radiation on cloud layer evolution are not as strong.
- Clouds with larger solar heating rates reduce negative buoyancy production and, thus constrain the depth of the circulations. Clouds with weaker solar heating rates have deeper and more vigorous circulations.
- Partitioning of radiant energy between the inversion zone and the mixed-layer is affected by the gradient in extinction at cloud top; this partitioning is likely dependent upon drop-distribution shape which helps determine the amount of buoyancy generated.

Because of the importance of ASC in regulating the Arctic heat budget through radiative effects, which impact such factors as equilibrium sea-ice thickness and feedbacks into climate (Curry et al., 1996), further studies of the radiative, microphysical and dynamical interactions associated with these clouds need to be undertaken. The strong SW heating that these clouds constantly endure appears to significantly affect cloud evolution and will thus impact the heat budget of the Arctic. This impact is likely to be highly dependent upon cloud top drop distribution dispersions which are affected by the amount of pollution aerosol and other environmental factors. Further studies which examine the effects of both shortwave and longwave feedbacks through microphysics will help elucidate the impact of potential pollution and warming events.

A host of factors not investigated in this paper, such as mesoscale subsidence and baroclinicity, advection, and large-scale dynamical forcing, also have a substantial

influence on the local character of ASC. Studying these effects and their interactions with the small-scale dynamics and microphysics considered herein will require either more complex time-varying and non-cyclic boundary conditions or an LES domain nested within a coarser grid. Ultimately, this work and future studies should provide guidance for parameterizations in large-scale models which can simulate the interactions of ASC with the large-scale arctic atmosphere/sea-ice/ocean system.

Acknowledgements

This research was supported by the Environmental Sciences Division of the U.S. Department of Energy (under contract number DE-FG03-95ER61958) as part of the Atmospheric Radiation Measurement Program which is part of the DOE Biological and Environmental Research (BER) Program. J. Harrington was supported by the Augmentation Awards for Science and Engineering Training under Contract F49620-95-1-0386. G. Feingold received support from the NASA/FIRE III program. P. Olsson received support in part from the Geophysical Institute, University of Alaska Fairbanks. The authors thank Bjorn Stevens for his assistance with the model development and two anonymous reviewers for their helpful comments.

References

Ackerman, A.S., Toon, O.B., Hobbs, P.V., 1993. Dissipation of marine stratiform clouds and collapse of the marine boundary layer due to the depletion of cloud condensation nuclei by clouds. Science 262, 226–229.

Albrecht, B.A., 1989. Aerosols, cloud microphysics and fractional cloudiness. Science 245, 1227–1230.

Barrie, L.A., 1986. Arctic air pollution: an overview of current knowledge. Atmos. Environ. 20, 643–663.

Berry, E.X., Reinhardt, R.L., 1974. An analysis of cloud drop growth by collection: Part IV. A new parameterization. J. Atmos. Sci. 31, 2127–2135.

Betts, A.K., 1973. Non-precipitating cumulus convection and its parameterization. Q. J. R. Meteorol. Soc. 99, 178–196.

Curry, J.A., 1986. Interactions among turbulence, radiation, and microphysics in Arctic stratus clouds. J. Atmos. Sci. 43, 90–106.

Curry, J.A., 1995. Interactions among aerosols, clouds, and climate of the Arctic Ocean. Sci. Total Environ. 160–161, 777–791.

Curry, J.A., Ebert, E.E., 1992. Annual cycle of radiative fluxes over the Arctic Ocean: sensitivity to cloud optical properties. J. Climate 5, 1267–1280.

Curry, J.A., Herman, G.F., 1985a. Relationships between large-scale heat and moisture budgets and the occurrence of Arctic stratus clouds. Mon. Weather Rev. 113, 1441–1457.

Curry, J.A., Herman, G.F., 1985b. Infrared radiative properties of summertime arctic stratus clouds. J. Climatol. Appl. Meteorol. 24, 525–538.

Curry, J.A., Ebert, E.E., Herman, G.F., 1988. Mean and turbulent structure of the summertime Arctic cloudy boundary layer. Q. J. R. Meteorol. Soc. 114, 715–746.

Curry, J.A., Rossow, W.A., Randall, D., Schramm, J.L., 1996. Overview of arctic cloud and radiation characteristics. J. Climate 9, 1731–1736.

Deardoff, J.W., 1981. On the distribution of mean radiative cooling at the top of a stratocumulus-capped mixed-layer. Quart. J. R. Met. Soc. 107, 191–202.

Edwards, J.M., 1996. Efficient calculation of infrared fluxes and cooling rates using the two stream equations. J. Atmos. Sci. 53, 1921–1932.

Feingold, G., Stevens, B., Cotton, W.R., Walko, R.L., 1994. An explicit cloud microphysical/LES model designed to simulate the Twomey effect. Atmos. Res. 33, 207–233.

Feingold, G., Stevens, B.S., Cotton, W.R., Frisch, A.S., 1996. The relationship between drop in-cloud residence time and drizzle production in a simulated stratocumulus cloud. J. Atmos. Sci. 53, 980–1006.

Frisch, A.S., Fairall, C.W., Snider, J.B., 1995. Measurement of stratus cloud and drizzle parameters in ASTEX with a K_α-band Doppler radar and a microwave radiometer. J. Atmos. Sci. 52, 2788–2799.

Harrington, J.Y., 1997. The effects of radiative and microphysical processes on simulated warm and transition-season Arctic stratus. PhD dissertation, Colorado State University, Fort Collins, CO, USA, 270 pp.

Hegg, D.A., Ferek, R.J., Hobbs, P.V., 1995. Cloud condensation nuclei over the Arctic Ocean in early spring. J. Appl. Meteorol. 34, 2076–2082.

Heintzenberg, J., Hansson, H.-C., Covert, D.S., Blanchet, J.-P., Ogren, J.A., 1986. Physical and chemical properties of Arctic aerosols and clouds. In: Stonehouse, B. (Ed.), Arctic Air Pollution. Cambridge Univ. Press, Cambridge, pp. 22–36.

Herman, G.F., Curry, J.A., 1984. Observational and theoretical studies of solar radiation in Arctic stratus clouds. J. Climatol. Appl. Meteorol. 23, 5–24.

Herman, G., Goody, R., 1976. Formation and persistence of summertime Arctic clouds. J. Atmos. Sci. 33, 1537–1553.

Houghton, J.T., Callendar, B.A., Varney, S.K. (Eds.), 1992. Climate Change 1992: The Supplementary Report to the IPCC Scientific Assessment. Cambridge Univ. Press, New York, 150 pp.

Hu, Y.X., Stamnes, K., 1993. An accurate parameterization of the radiative properties of water clouds suitable for use in climate models. J. Climate 6, 728–742.

Lilly, D.K., 1968. Models of cloud-topped mixed layers under a strong inversion. Q. J. R. Meteorol. Soc. 94, 292–309.

Liou, K.N., 1992. Radiation and Cloud Processes in the Atmosphere. Oxford Univ. Press, New York, 487 pp.

Mitchell, D.L., 1997. Parameterization of the Mie extinction and absorption coefficients: a process oriented approach. Appl. Opt., submitted.

Nicholls, S., 1988. The structure of radiatively driven convection in stratocumulus. Q. J. R. Meteorol. Soc. 115, 487–511.

Pielke, R.A., Cotton, W.R., Walko, R.L., Tremback, C.J., Lyons, W.A., Grasso, L.D., Nicholls, M.E., Moran, M.D., Wesley, D.A., Lee, T.J., Copeland, J.H., 1992. A comprehensive meteorological modeling system—RAMS. Meteorol. Atmos. Phys. 49, 69–91.

Randall, D.A., 1980. Conditional instability of the first kind upside down. J. Atmos. Sci. 37, 125–130.

Ritter, B., Geleyn, J.-F., 1992. A comprehensive radiation scheme for numerical weather prediction models with potential application in climate simulations. Mon. Weather Rev. 120, 303–325.

Rogers, D.P., Koračin, D., 1992. Radiative transfer and turbulence in the cloud-topped marine atmospheric boundary layer. J. Atmos. Sci. 49, 1473–1486.

Saxena, V.K., Rathore, R.S., 1984. Transport and formation of summertime cloud condensation nuclei over the Arctic Ocean. 11th International Conference on Atmospheric Aerosols, Condensation, and Ice Nuclei in Budapest, Hungary. International Association for Meteorology and Atmospheric Physics, pp. 292–298.

Shaw, G.E., 1986. Aerosols in Arctic air masses. J. Atmos. Chem. 4, 157–171.

Slingo, A., Schrecker, H.M., 1982. On the shortwave radiative properties of stratiform water clouds. Q. J. R. Meteorol. Soc. 108, 407–426.

Stamnes, K., Zak, B., Shaw, G.E., 1995. The Atmospheric Radiation Measurements (ARM) program: ARM's window on the Arctic. Sci. Total Environ. 160–161, 825–829.

Stevens, B., 1996. On the dynamics of precipitating stratocumulus. PhD dissertation, Colorado State University, 140 pp.

Stevens, B., Feingold, G., Walko, R.L., Cotton, W.R., 1996. On elements of the microphysical structure of numerically simulated non-precipitating stratocumulus. J. Atmos. Sci. 53, 980–1006.

Tripoli, G.J., Cotton, W.R., 1981. The use of ice-liquid water potential temperature as a thermodynamic variable in deep atmospheric models. Mon. Weather Rev. 109, 1094–1102.

Tsay, S.-C., Jayaweera, K., 1984. Physical properties of Arctic stratus clouds. J. Climatol. Appl. Meteorol. 23, 584–596.

Twomey, S., 1959. The nuclei of natural cloud formation: Part II. The supersaturation in natural clouds and the variation of cloud droplet concentration. Geofis. Pura Appl. 43, 243–249.

Tzivion, S., Feingold, G., Levin, Z., 1987. An efficient numerical solution to the stochastic collection equation. J. Atmos. Sci. 44, 3139–3149.

Walko, R.L., Cotton, W.R., Meyers, M.P., Harrington, J.Y., 1995. New RAMS cloud microphysics parameterization: Part I. The single moment scheme. Atmos. Res. 38, 29–62.

Walsh, J.E., Crane, R.G., 1992. A comparison of GCM simulations of Arctic climate. Geophys. Res. Lett. 19, 29–32.